The Karhunen–Loéve decomposition of minimal channel flow

G. A. Webber
Center for Fluid Mechanics, Brown University, Providence, Rhode Island 02912

R. A. Handler
Naval Research Laboratory, Washington, DC 20375

L. Sirovich
Center for Fluid Mechanics, Brown University, Providence, Rhode Island 02912

Minimal channel flow is analyzed by means of the Karhunen–Loéve (KL) decomposition. It is shown that the most energetic modes are streamwise rollers followed by outward tilted quasi-streamwise vortices. Both of these mode types have a strong similarity to structures seen in physical experiments. Temporal plots of roll energy, propagating energy, bulk velocity, and representational entropy have been obtained. Study of the evolution of these variables shows a consistent pattern of growth and decay in which entropy plays a key role in describing the events in the turbulent process. The roll and propagating modes are also shown to make independent contributions to the Reynolds stress with the roll modes dominating the profile near the walls and the propagating modes having larger values towards the channel center. A comparison of the KL dimension of this flow and a full channel flow shows that the dimension scales with box size, i.e., it confirms the assertion that dimension is an extensive variable. © *1997 American Institute of Physics.* [S1070-6631(97)00503-5]

I. INTRODUCTION

The fundamental physics of wall bounded turbulence is conveniently studied through channel flow, i.e., flow between two parallel plates and driven by a uniform pressure gradient. The simplicity of the channel flow geometry allows for direct numerical simulations at low Reynolds numbers which provide an abundance of accurate flow data. In this work, we will define *minimal channel* to be the narrowest channel for fixed length in which turbulence is maintained on both walls. Jiménez and Moin, who first studied such flows, found that channels of narrower extent produced either one walled turbulence or in extreme cases the flow relaminarizes.[1] The minimal channel flow was originally designed to establish ''a significantly simpler and more manageable 'laboratory' in which to study the mechanics of wall-bounded flows.''[1] In this work, we intend to use this ''laboratory'' to further study wall-bounded turbulence by decomposing the flow into its dominant modes. For the purposes of the current study, we consider the minimal channel flow to possess all the dynamics needed to produce turbulence with the least repetition of structure. We anticipate that this flow takes place on a lower dimensional attractor than other turbulent channel flows at a given Reynolds number. In this regard we may expect the clearest identification of fundamental turbulent mechanisms. Here we use the Karhunen–Loéve procedure to produce an optimal basis set which best represents the turbulent activity of the minimal channel flow. Using these functions, we intend to study the birth, growth, and destruction of turbulent structures by examining the the evolution of these KL modes. To place this work in context, we now briefly review the current view of wall-bounded turbulence.

In the last several decades, a relatively simple physical picture has emerged which attempts to describe the vorticity dynamics responsible for maintaining wall-bounded turbulence. We should preface the description of the so called *standard model* by remarking that details of such models are not universally accepted, and many of the ideas are currently undergoing revision and rethinking. In one scenario, which is typical of a class of models that have been developed, vortex dynamics plays a central role. One first observes that as a result of the mean streamwise velocity profile, at any instant in time, the wall region can be thought of as an ensemble of vortex lines aligned principally in the spanwise direction. The turbulence will naturally induce random kinks in the spanwise oriented vortex lines, some of which (the kinks) possess a curvature which induces lift into a region of higher streamwise velocity. This will result in the stretching and therefore the intensification of the vorticity. At this point, the configuration of the vortex line is that of a *hairpin*, the *legs* of which are oriented in the streamwise direction.[2] Near the tip of the hairpin, sometimes referred to as the *head*, there is a strong upward *ejection* of fluid on the inner part of the tip, and an equally strong wallward *sweep* on the outer part. This configuration generates a spanwise shear-layer, which is evidenced by an inflexional instantaneous mean velocity profile.[3] The flow is then thought to undergo an instability on account of the strong mean shear layer which is the source of a violent generation of small scale turbulence, the event being termed a *burst*. The small scale turbulence generated during such a burst can then initiate the start of the next cycle. A schematic of the scenario is presented by Hinze.[4]

Several remarks are now in order about this generic scenario which may be termed the *ejection-burst-sweep* cycle. Though there may be disagreements on details of the scenario, certain views appear to be nearly universally accepted. The first is the observation that the flow is quasi-periodic in the spanwise (x_3) direction with a characteristic wavelength,

λ^+, of approximately $100\delta_\tau$, where the wall unit, $\delta_\tau = \nu/u_\tau$, ν is the kinematic viscosity, and u_τ is the viscous velocity based on wall shear stress and density. Flow visualization studies[5,6] reveal elongated near-wall streaks whose streamwise extent can often exceed $1000\delta_\tau$. In addition, the temporal duration of a *burst* and the time between them have been well characterized.[7] In studying the life of these streaks, Bernard, Thomas, and Handler[8] identify what they call quasi-streamwise vortices which are shorter than the streaks and are tilted away from the wall. Extensive experiments and simulations have established the peak of the root mean square departure from the mean streamwise velocity to be located approximately at $x_2^+ \approx 15$,[9,10] where $x_2^+ = x_2 u_\tau / \nu$ and x_2 is the wall normal coordinate. Finally, for fully developed wall turbulence, the mean velocity profile exhibits four distinct regions; sub-layer, buffer region, log-layer, and a turbulent core,[11] with maximal turbulence production occurring at $x_2^+ \approx 13.5$.

A difficulty in identifying *coherent structures* for wall-bounded turbulent flows, e.g., the quasi-streamwise vortices mentioned above, lies in the imprecision and subjectivity in defining it. In a very broad way, however, the term refers to some flow structure perhaps formed by the concentration of vorticity, the structure itself undergoing a stereotypical temporal evolution involving birth, growth, and eventual decay. This description, however, is almost certainly inadequate or of little practical value, in the sense that each turbulent flow seems to possess its own kinds of coherent structures which become evident upon close examination of the flow. In any event, the idea that coherent structures are closely tied to the kinematic notion of a concentration of vorticity seems inescapable, along with the idea that such structures are found throughout the flow at any given instant and seem to have temporal lifetimes longer than one would associate with random background vorticity.

In the case of wall-bounded turbulence, there is almost universal agreement that such coherent structures do exist. The question that arises immediately is whether one can take advantage of their existence in the computation, modeling, and understanding of the flow. In more precise terms, the Navier–Stokes equations are infinite dimensional but empirical evidence suggests that the system can be described by a finite, and possibly small number of degrees of freedom—a low-order dynamical system. A first step in the determination of such a system, if one actually exists, is to identify an *optimal coordinate system* in which to describe the turbulence. A method was proposed by Lumley[12] based on the classical work of Karhunen,[13] and Loéve.[14] (The method goes back to Schmidt;[15] see Ref. 16 for a history.) The idea is that the flow field itself (velocity, vorticity, etc.) be used to define this coordinate system in a precise mathematical way. This procedure, termed the Karhunen–Loéve (KL) decomposition, has found broad use in pattern recognition,[17] and in geophysics[18] and has been alternately called the proper orthogonal decomposition (POD, Ref. 14), the empirical orthogonal function (EOF, Ref. 19) analysis, and empirical eigenfunction analysis (EEF, Ref. 20).

The geometrical simplicity of channel flow makes it ideal for the application of Karhunen–Loéve analysis. From the translational invariance of the flow, all eigenfunctions are sinusoidal in the streamwise and spanwise directions. Further symmetries recognized by Sirovich[21] show, among other properties, that modes are even or odd around the horizontal midplane. The earliest application of KL analysis to numerically obtained channel flow data was performed by Moin and Moser[22] with attention paid to the construction of a dominant eddy of the flow. In a separate study by Sirovich, Ball, and Keefe,[23] various structures are identified along with their behavior over time. The most energetic modes are found to have no streamwise dependence. In addition, a set of modes were discovered which moved at steady and predictable speeds at oblique angles to the streamwise direction. Related papers by Ball, Sirovich, and Keefe[24] and Sirovich, Ball, and Handler[25] show how these mode types make unique contributions to the flow statistics over time. That work also suggests that these ''propagating'' modes play an essential role in the bursting process found in wall-bounded turbulence.

Recent attempts to develop low-order dynamical systems for these flows using the Karhunen–Loéve eigenfunctions as a basis set have given rise to models which mimic in some important respects the original Navier–Stokes system. In the first use of the empirical eigenfunctions to obtain a dynamical system, Sirovich and Rodriguez[26] obtained excellent results for the Ginzburg–Landau model. It is important, however, to place this preliminary success in the context of a real fluid calculation,[27] which showed that wall-bounded turbulence is governed by a strange attractor whose dimension, even for low Reynolds numbers, is sobering (viz. for a friction Reynolds number of 80 the dimension is about 780). This result alone might suggest an end to the pursuit of a low-order description of wall-bounded turbulence and other open turbulent flows. However, it is not obvious that one needs to accurately represent all modes to gain insight into the principal underlying dynamics.[28] In this respect, these models should be viewed as idealizations—Sirovich and Zhou[29] describe them as *impressionistic*. Models can be thought of as test-beds for trying out novel methods of active turbulence control, and for understanding the mechanisms involved in turbulent drag reduction by riblets[30] and by polymer addition.[31] For example, recent simulations[32] have shown that perturbation of the wave-like modes described above, significantly reduces drag in fully developed turbulent channel flow and produces turbulence statistics remarkably similar to those found in polymer-induced drag reduction. Based on the KL analysis of the minimal channel flow, to be presented in this paper, we find reason for optimism that concepts from dynamical systems theory will yield a more fundamental understanding of wall-bounded turbulence and perhaps even the means to control it.

The minimal channel used in this work, with a spanwise width of $L_3 = 128\delta_\tau$, can also be viewed in the framework of the wide channel[25] which has a spanwise width of $L_3 = 640\delta_\tau$. In natural coordinates the largest wavelength in the spanwise direction is L_3, and corresponds to the sinusoidal wave number $n = 1$. Suppose we perform a numerical experiment in the large channel such that the initial condition contains only the spanwise wave number $n = 5$, then the Navier–Stokes system respects this symmetry and the only

Phys. Fluids, Vol. 9, No. 4, April 1997

Webber, Handler, and Sirovich   1055

wave numbers which will emerge in the evolution of the flow are multiples of $n=5$, i.e. $n=0,\pm 5,\pm 10,\pm 15,\ldots$. This result follows from an examination of the triad interactions of the Navier–Stokes equations (see Ref. 29 for a more complete explanation). Thus, the same solution could also have been achieved by studying a channel flow of width $L_3=128\delta_\tau$, one fifth the original spanwise width, and the usual spanwise periodic conditions. Thus the minimal channel is seen to be that slice of the wide channel for which just one roll pair appears. An important distinction between the narrow and full channels appears if one compares their eigenvalue spectra. For example, the mode which corresponds with the streak spacing for the large channel ($n=5$) appears fourth in rank (see Table I) whereas the same mode ($n=1$) for the minimal channel appears first. As mentioned in Ref. 29, the streamwise independent modes represent a form of two dimensional turbulence, and thus can be expected to undergo an inverse cascade. Therefore there is a tendency for the $n=5$ mode to migrate to smaller wave number modes, and this is borne out by the eigenvalue spectrum. This observation underlines the fact that the narrow channel is only a model of the full flow, and that it is inaccurate in regard to important dynamical effects. On the other hand, since dimension is an extensive quantity, the narrower channel has an attractor dimension which is roughly one fifth the dimension of the wide channel, if both had the same length. These considerations lead to the conclusion that the minimal channel is a significantly simpler system to use in exploring the dynamics of wall bounded turbulence.

II. NUMERICAL METHODS

A. Turbulence simulation

We simulate the flow in a channel by solving the incompressible Navier–Stokes equation in rotation form given by

$$\frac{\partial \mathbf{U}}{\partial t}=\mathbf{U}\times\mathbf{\Omega}-\frac{1}{\rho}\mathbf{\nabla}\Pi+\frac{1}{R_\tau}\nabla^2\mathbf{U}+1\,\mathbf{e}_1, \tag{1}$$

$$\mathbf{\nabla}\cdot\mathbf{U}=0, \tag{2}$$

and the boundary condition is

$$\mathbf{U}=0,\qquad x_2=\pm 1 \tag{3}$$

where $\mathbf{U}(\mathbf{x},t)$ is the velocity, $\mathbf{\Omega}$ is the vorticity, $\Pi=p+\frac{1}{2}\rho|\mathbf{U}\cdot\mathbf{U}|^2$, p is the pressure, and ρ is the density. We use the notation (x_1,x_2,x_3) to denote the streamwise, wall normal, and spanwise coordinates, respectively. Velocity is scaled by the friction velocity $u_\tau=\sqrt{\tau_w/\rho}$ where τ_w is the viscous shear at the wall, $\mathbf{x}$ is scaled by the half width of the channel, h, time is scaled by h/u_τ, and R_τ, the friction Reynolds number, is given by $R_\tau=u_\tau h/\nu$, where ν is the kinematic viscosity. We can refer to velocity, length, and time in local wall units expressed as $u^+=u/u_\tau$, $\mathbf{x}^+=\mathbf{x}/\delta_\tau$, and $t^+=tu_\tau/\delta_\tau$. For the remainder of the paper, it is understood that quantities with the superscript ($+$) are reported in wall units. In our calculations, the applied pressure gradient remains constant and is given by $1\,\mathbf{e}_1$ where $\mathbf{e}_1$ is the unit vector in the streamwise direction.

To solve Eqs. (1)–(3), we use the numerical methods developed by Kim, Moin, and Moser[10] in which the velocity field is approximated by a Fourier–Chebyshev expansion which can be written as

$$\mathbf{U}(\mathbf{x},t)=\sum_{m=-M/2}^{M/2-1}\sum_{n=-N/2}^{N/2-1}\sum_{p=0}^{P}\mathbf{a}_{mnp}(t)$$
$$\times T_p(x_2)e^{ik_1x_1}e^{ik_3x_3}, \tag{4}$$

where $T_p(x_2)$ denotes the Chebyshev polynomials, $k_1=2\pi m/L_1$, and $k_3=2\pi n/L_3$, where L_1 and L_3 are the domain lengths in the x_1 and x_3 directions, respectively. The initial conditions were obtained from previous simulations of fully developed turbulence performed by Handler, Hendricks, and Leighton.[33] In our simulations, the box lengths were set to $L_1=\pi$ and $L_3=0.3\times\pi$, and the resolution was $129\times48\times24$ in the wall normal, streamwise, and spanwise directions, respectively. The friction Reynolds number was set to 135.5 which was so chosen as to maintain a bulk Reynolds number, $Re_b=3U_bh/2\nu$, of 3000 as determined from the results of Dean[34] where the bulk velocity U_b is the average velocity across the cross-section of the duct,

$$U_b(t)=\frac{1}{A}\int_A\mathbf{U}(\mathbf{x},t)dA, \tag{5}$$

and A is the cross-sectional area. It is known from the simulations of Jiménez and Moin that this domain should lead to a self sustaining turbulence which is confirmed in our simulations.

B. Karhunen–Loéve decomposition

In applying the Karhunen–Loéve or proper orthogonal decomposition (POD) to turbulent channel flow, we first separate the velocity field, $\mathbf{U}$, into a mean and fluctuating portion, $\mathbf{u}$, as follows:

$$\mathbf{U}(x_1,x_2,x_3,t)=U(x_2)\mathbf{e}_1+\mathbf{u}(x_1,x_2,x_3,t), \tag{6}$$

where $U(x_2)$ is the mean obtained by averaging over the horizontal (x_1,x_3) plane and time. It is important for our subsequent deliberations to recognize that averaging over a horizontal plane does not yield a time independent statistic, unless that area can be made to approach infinity. Virtually all simulations produce a $U_b(t)$, (5), which is time dependent. Henceforth, it is understood that the eigenfunctions are obtained from the fluctuating portion only.

The velocity field, $\mathbf{u}(x_1,x_2,x_3,t)$ is homogeneous in the x_1 and x_3 directions so that the data set can be enlarged by including an additional flow field $\mathbf{u}(x_1+l_1,x_2,x_3+l_3,t)$ for each value of l_1 and l_3, that is the velocity field is translationally invariant in the horizontal plane. This implies sinusoidal dependence in the horizontal plane and allows for a direct KL analysis on $\hat{\mathbf{u}}(x_2,m,n)$ which is the Fourier transform of $\mathbf{u}$ in the x_1 and x_3 directions. The effective size of the data set can be increased by a factor of four by including reflectional symmetries around the midplane, $x_2=0$, and the vertical plane, $x_3=L_3/2$, and a 180° rotational symmetry around the channel center, $x_2=0,x_3=L_3/2$.[21] It follows that

Webber, Handler, and Sirovich

for each wave number index pair, (m,n), the empirical eigenfunctions, ψ, and eigenvalues, λ, are determined from the equation

$$\int_{-h}^{h} \kappa_{ij}(x_2,x_2',m,n)\psi_j(x_2',m,n)dx_2' = \lambda(m,n)\psi_i(x_2),$$

$$i,j = 1,2,3, \tag{7}$$

where $\kappa_{ij}(x_2,x_2',m,n)$ is the two point spatial correlation tensor or covariance matrix formed from

$$\kappa_{ij}(x_2,x_2',m,n) = \langle \hat{u}_i(x_2,m,n)\bar{u}_j(x_2',m,n) \rangle, \tag{8}$$

where the expectation is taken over all realizations and symmetries, and the bar denotes the complex conjugate. In order to solve the eigenvalue problem, a discretization must first be performed in the x_2 direction.[24] Our geometry uses 129 points resulting in 387 (3×129) eigenvalues and eigenfunctions for each wave number index pair. Using the quantum number q to specify an eigenfunction for a wave number index pair, the triplet $\mathbf{k} = (m,n,q)$ completely specifies an eigenfunction.

The three dimensional eigenfunction is a complex valued vector field which can be written as

$$\boldsymbol{\phi}^{\mathbf{k}}(x_1,x_2,x_3) = \boldsymbol{\psi}^{\mathbf{k}}(x_2,m,n)e^{2\pi imx_1/L_1}e^{2\pi inx_3/L_3}. \tag{9}$$

It is important to note some properties retained by the eigenfunctions. First, because the eigenfunctions are derived from physical flow fields, they are themselves flow fields and retain the incompressibility property, $\nabla \cdot \boldsymbol{\phi}^{\mathbf{k}} = 0$. The eigenfunctions also satisfy the no slip boundary condition, $\boldsymbol{\phi}^{\mathbf{k}} = 0$ at $x_2 = \pm h$. It follows from the Hermitian property of $\kappa_{ij}(x_2,x_2',m,n)$ that the eigenfunctions are orthonormal,

$$\int_D \boldsymbol{\phi}^{\mathbf{k}} \cdot \overline{\boldsymbol{\phi}}^{\mathbf{l}} d\mathbf{x} = \delta_{\mathbf{kl}}, \tag{10}$$

and the eigenvalues must all be real. This allows any velocity field to be decomposed as a linear superposition of the eigenfunctions $\mathbf{u}(\mathbf{x},t) = \Sigma_{\mathbf{k}} a^{\mathbf{k}}(t)\boldsymbol{\phi}^{\mathbf{k}}(\mathbf{x})$, where the coefficients are obtained from

$$a^{\mathbf{k}}(t) = \int_D \mathbf{u}(\mathbf{x},t) \cdot \overline{\boldsymbol{\phi}}(\mathbf{x})^{\mathbf{k}} d\mathbf{x}. \tag{11}$$

It is straightforward to show that the eigenvalues, λ, which represent the energy in each KL mode, can be obtained from the coefficients by

$$\lambda^{\mathbf{k}} = \left\langle \left| \int_D \mathbf{u} \cdot \overline{\boldsymbol{\phi}}^{\mathbf{k}} d\mathbf{x} \right|^2 \right\rangle = \langle a^{\mathbf{k}}(t)\bar{a}^{\mathbf{k}}(t) \rangle. \tag{12}$$

It follows from the flow symmetries discussed earlier and the reality of the flow that all eigenfunctions can be found from the solutions calculated in wave number space $m \geq 0, n \geq 0$. From this, it is easy to show that an eigenvalue $\lambda^q(m,n)$ is equal to eigenvalues in the other quadrants $\lambda^q(-m,n)$, $\lambda^q(m,-n)$, and $\lambda^q(-m,-n)$. Degeneracy, $d^{\mathbf{k}}$, denotes the multiplicity of such eigenvalues. Degeneracy is equal to four if $m \neq 0$ and $n \neq 0$, equal to two if one but not both m,n are equal to 0, and equal to one if $m = 0$ and $n = 0$. In order to account for all wave number index pairs,

the energy, $e^{\mathbf{k}} = d^{\mathbf{k}}\lambda^{\mathbf{k}}$, is calculated and this represents the energy in all corresponding eigenfunctions. An energy fraction, $f^{\mathbf{k}} = e^{\mathbf{k}}/\Sigma_{\mathbf{k}'}e^{\mathbf{k}'}$, determines the portion of energy in any mode, and after ordering the modes from largest to smallest, a cumulative energy can be calculated,

$$s^p = \sum_{\mathbf{k}}^{p} f^{\mathbf{k}}, \qquad \mathbf{k} = (m,n,q), \qquad f^{\mathbf{k}} > f^{\mathbf{k}+1}, \tag{13}$$

which represents the portion of energy in the most energetic group of p modes.

Along with these time averaged quantities, the decomposition properties are used to compute some important temporal statistics. It will be useful in what follows to define $E(t)$ equal to twice the fluctuating kinetic energy from the relation

$$E(t) = \int_D \mathbf{u}(\mathbf{x},t) \cdot \mathbf{u}(\mathbf{x},t)d\mathbf{x} = \sum_{\mathbf{k}} a^{\mathbf{k}}(t)\bar{a}^{\mathbf{k}}(t). \tag{14}$$

Using this, we define the probability

$$p^{\mathbf{k}}(t) = a^{\mathbf{k}}\bar{a}^{\mathbf{k}}(t)/E(t), \tag{15}$$

for each mode. This probability represents the portion of energy in any mode, $\mathbf{k}$. Finally, a representational entropy, $S(t)$, is computed which calculates the degree to which the energy is distributed over the modes:

$$S(t) = -\sum_{\mathbf{k}} p^{\mathbf{k}}(t)\ln(p^{\mathbf{k}}(t)). \tag{16}$$

A small value of S indicates that few modes contain the bulk of the energy while a large value of S indicates that the energy is distributed over many modes. While the flow can be decomposed into any orthonormal basis set, it has been shown by Sirovich[35] that the empirical eigenfunctions are the basis set which minimizes the representational entropy for the time averaged probabilities.

III. RESULTS

A. Turbulence statistics

Using the methods and parameters defined in Sec. II, we have simulated turbulence in a minimal channel for a time of approximately $29h/u_\tau$ or $t^+ = 4000$. At this Reynolds number and box size, Jiménez and Moin[1] find fully developed turbulent activity on both walls. Our results agree with theirs with both walls maintaining activity through the majority of the simulation. At a lower bulk Reynolds number or box size they find turbulent activity on only one wall, which switches in an intermittent fashion from one wall to the other. We note that the turbulent activity on one wall tended to dominate over the other through some portions of the simulation, but this effect did not cause a noticeable asymmetry in the mean velocity profile or any other statistics that we examined. Another point of interest is that we drive the flow with a constant pressure gradient while Jiménez and Moin used a constant mass flux condition. With the exception of the mean velocity profile, as we will discuss below, this difference in driving mechanisms did not affect the statistics in any significant way compared to those found by Jiménez and Moin.
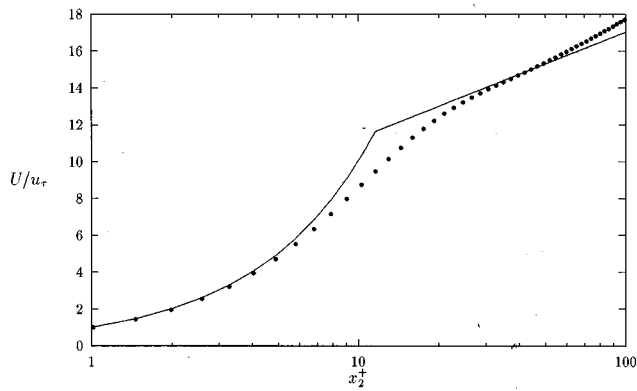
FIG. 1. Mean streamwise velocity near the wall. Solid line is $U/u_\tau = 2.5 \ln x_2^+ + 5.5$, point values are results of the minimal channel simulation.

FIG. 3. Power spectra of the velocity vs the streamwise index, m, on the plane $x_2^+ = 14.5$. The solid line represents u_1, the small dots represent u_2, and the bold dots represent u_3.

With the given pressure gradient used in our simulation, we achieve a time averaged bulk Reynolds number of $Re = \frac{3}{2}(U_b h/\nu)$ and a centerline Reynolds number, $Re_{cl} = U_{cl} h/\nu$, of 2489. These values are close to the correlations of Dean[34] with our bulk Reynolds number exceeding Dean's prediction by 3%. We note in Fig. 1, that the mean profile exceeds the classical law of the wall results, and it should be noted that Jiménez and Moin find similar results. They observe that the difference seems to occur in the center of the channel and could be related to the formation of large structures. As additional support, we observe that the argument leading to the log law follows from the assumptions $x_2^+ \gg 1$ and $x_2^+ \ll R_\tau$. Next we note that the minimal channel has the additional restriction that the width of the channel is roughly $128\delta_\tau$. An individual roll is half this, or $64\delta_\tau$. This last estimate imposes the estimate that $x_2^+ \ll 64$ which makes it unlikely that a log layer will appear even if $R_\tau \uparrow \infty$.

The root mean square velocity fluctuations, $u_1' = \langle u_1^2 \rangle^{1/2}$, $u_2' = \langle u_2^2 \rangle^{1/2}$, $u_3' = \langle u_3^2 \rangle^{1/2}$, are shown in Fig. 2 along with empirical results of Wei and Willmarth at a Reynolds number of $Re_{cl} = 2970$. It is evident that our results compare quite well with those of Wei and Willmarth. Energy
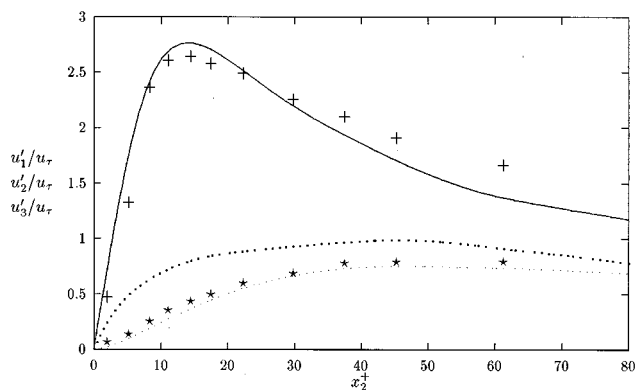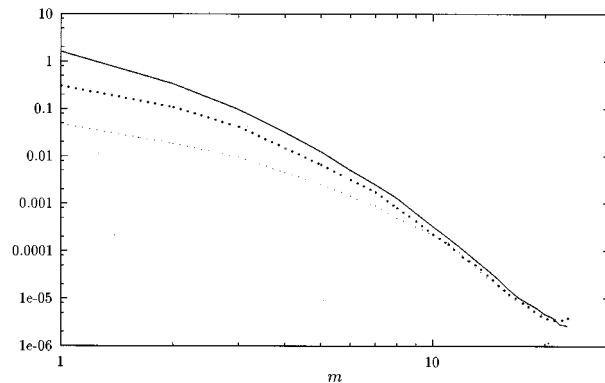
spectra, shown in Figs. 3 and 4, show decays of 3 to 5 orders of magnitude indicating the flow to be well resolved spatially.

The results of Figs. 1–4 clearly show that our results compare well with classical experimental results and those of Jiménez and Moin, and as such, the minimal flow unit provides a sound basis for the study of wall-bounded turbulence. The minimal channel turbulence is fully self-sustaining, two walled, and produces accurate statistics while isolating the dominant flow structures. We believe that this allows for a clear examination of the relevant structures.

B. Decomposition of the minimal channel flow

We identify the dominant structures by applying the Karhunen–Loéve decomposition, as described in Sec. II, to the minimal channel flow examined above. A listing of the first fifteen modes is presented in Table I along with a comparison to the full channel flow calculated by Sirovich, Ball, and Handler[25] at nearly the same Reynolds number. The cumulative energy sum for the two flows, as described in (13), are also compared in Fig. 5. A first conclusion that can be drawn from these results is that the minimal channel is of
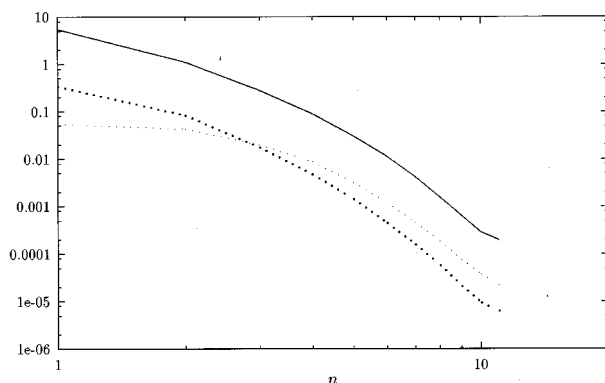

FIG. 2. Root mean squared fluctuations. Solid line, u_1'/u_τ: small dots, u_2'/u_τ: large dots, u_3'/u_τ, $Re_{cl} = 2489$. Symbols are data from Wei and Willmarth[9] at $Re_{cl} = 2970$. Wei and Willmarth did not measure u_3'.

FIG. 4. Power spectra of the velocity vs the spanwise index, n, on the plane $x_2^+ = 14.5$. The solid line represents u_1, the small dots represent u_2, and the bold dots represent u_3.

TABLE I. Energy content of the first 15 eigenfunctions of the minimal channel flow and the full channel flow.

| Index | Minimal channel $R\tau = 135.5$ | | | Full channel $R\tau = 125$ | | |
	Mode (m,n,q)	Energy fraction	Energy sum	Mode (m,n,q)	Energy fraction	Energy sum
1	(0,1,1)	0.13275	0.13275	(0,3,1)	0.04282	0.04282
2	(0,1,2)	0.10473	0.23748	(0,1,1)	0.03990	0.08272
3	(1,1,1)	0.04863	0.28611	(0,4,1)	0.03266	0.11539
4	(1,1,2)	0.04807	0.33418	(0,5,1)	0.02866	0.14405
5	(0,1,3)	0.02937	0.36355	(0,4,2)	0.02288	0.16693
6	(0,1,4)	0.02170	0.38525	(0,1,2)	0.02097	0.18790
7	(1,1,3)	0.01899	0.40425	(0,3,2)	0.02064	0.20855
8	(1,1,4)	0.01721	0.42145	(0,2,1)	0.01967	0.22822
9	(0,0,1)	0.01700	0.43845	(0,2,2)	0.01878	0.24700
10	(2,1,1)	0.01651	0.45496	(0,6,1)	0.01381	0.26082
11	(0,2,1)	0.01376	0.46872	(0,5,2)	0.01310	0.27392
12	(1,0,1)	0.01348	0.48220	(1,3,1)	0.01252	0.28645
13	(0,0,2)	0.01338	0.49586	(1,2,1)	0.00948	0.29593
14	(1,2,1)	0.01328	0.50886	(1,4,1)	0.00837	0.30430
15	(1,2,2)	0.01289	0.52175	(1,5,1)	0.00829	0.31258

lower dimension with fewer modes needed to account for any fraction of the energy. This result supports the expectation that the minimal channel has less structural repetition than the full channel making the fundamental turbulent mechanisms easier to identify.

In order to evaluate the dimension of a flow, which allows it to be compared to other flows, we use the nominal KL dimension as defined by Sirovich.[35] The KL dimension, D_{KL}, denotes the number of modes, including degeneracies, which are needed to account for 90% of the energy in the flow. We will examine the relationship between D_{KL} and box size by comparing the results of the minimal channel flow to those of the full channel flow. For the minimal channel, $D_{KL} = 658$ while the full channel has a KL dimension of 4186. In order to compare box size, we calculate the volume of each box in viscous units, δ_τ^3. The minimal channel, with a half height of $135.5\delta_\tau$, has a height of $271\delta_\tau$ between the two walls. This same channel has a streamwise length of

FIG. 5. Cumulative energy sum, s^p. The solid line is from the minimal channel flow, the dots are from the full channel flow calculated by Sirovich, Ball, and Handler.

$\pi \times 135.5\delta_\tau$ or $426\delta_\tau$ and a spanwise width of $0.3 \times \pi \times 135.5\delta_\tau$ or $128\delta_\tau$ resulting in a volume of $1.47 \times 10^7 \delta_\tau^3$. A similar calculation of the full channel shows its volume to be $9.77 \times 10^7 \delta_\tau^3$. The ratio of D_{KL} for the two flows is 0.157 while the ratio in volumes is 0.151, the two ratios differing by only 4%. The fact that these ratios are in such close agreement indicates that the KL dimension scales in proportion to volume which is in agreement with the assertion that dimension is an extensive variable. This suggests that a minimal channel version of the Keefe et al.[27] calculation would lead to a Lyapunov dimension of ~ 260 instead of ~ 780.

With the empirical eigenfunctions in hand, we use them to decompose and reconstruct the flow fields for storage and examination of the flow. A direct way to store a flow field is by its representation in physical space, for example, three components of velocity stored at each spatial point. Instead, we can use the empirical eigenfunctions to calculate the coefficients $a^k(t)$ as described in Eq. (11) and store these at discrete times. While the space needed to store all coefficients is the same as that needed to store the flow field in physical space, we choose to store the 3025 most energetic modes which account for 96.4% of the energy. This requires only 0.4% of the space needed for pointwise storage and represents a significant data compression. We note that a one time storage of the ''library'' of eigenfunctions is also necessary. To reconstruct the velocity field, $\mathbf{u}(\mathbf{x},t)$, an eigenfunction, $\boldsymbol{\phi}^{(m,n,q)}(\mathbf{x})$, will make its contribution to the flow, $\mathbf{u}^{(m,n,q)}(\mathbf{x},t)$, through as many as four degeneracies (fewer if either m or n is zero) which is written as

$$\mathbf{u}^{(m,n,q)}(\mathbf{x},t) = a^{(m,n,q)}(t)\boldsymbol{\phi}^{(m,n,q)}(\mathbf{x})$$
$$+ a^{(m,-n,q)}(t)\boldsymbol{\phi}^{(m,-n,q)}(\mathbf{x})$$
$$+ a^{(-m,n,q)}(t)\boldsymbol{\phi}^{(-m,n,q)}(\mathbf{x})$$
$$+ a^{(-m,-n,q)}(t)\boldsymbol{\phi}^{(-m,-n,q)}(\mathbf{x}). \quad (17)$$

Since this represents the summation of complex conjugate functions, $\mathbf{u}^{(m,n,q)}(\mathbf{x},t)$ fulfills the reality condition. In addition, since the eigenfunctions are derived from an actual incompressible flow, the reconstructed flow field, $\mathbf{u}^{(m,n,q)}(\mathbf{x},t)$, is incompressible and satisfies the no-slip boundary conditions, as well as periodic boundary conditions in the streamwise and spanwise directions. For a full reconstruction of the flow $\mathbf{u}(\mathbf{x},t)$, summation must be performed over the Fourier and quantum numbers,

$$\mathbf{u}(\mathbf{x},t) = \sum_m \sum_n \sum_q \mathbf{u}^{(m,n,q)}(\mathbf{x},t). \quad (18)$$

In addition to reconstructing the flow from all modes, insight can be gained by consideration of various groups of modes, such as the 100 most energetic modes, or even a single mode.

In Fig. 6, we show two surfaces (one positive and one negative) of constant streamwise vorticity at an instant in time. This is a reconstruction from all 3025 stored modes and can be considered to be a true flow realization. The vorticity field shows significant small scale activity making the identification of dominant structures difficult. By examining a
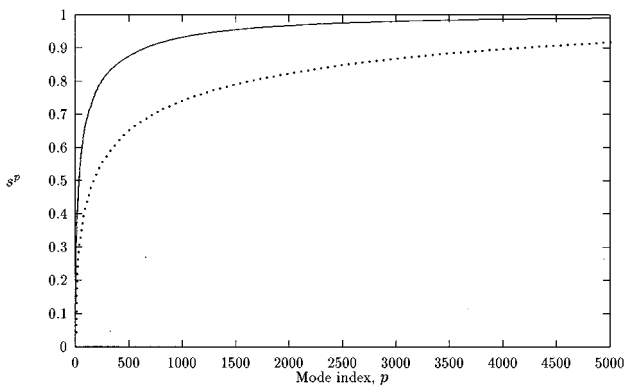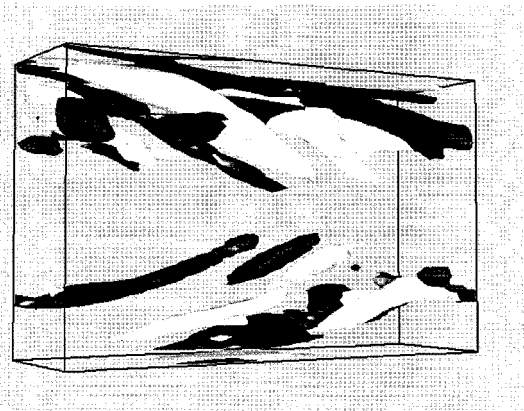
FIG. 6. Surfaces of constant streamwise vorticity from minimal channel reconstructed from all 3025 modes. The light surfaces are positive streamwise vorticity and dark surfaces are negative streamwise vorticity. The no slip planes are on the top and bottom, and the streamwise direction is from left to right.

FIG. 8. Surface of constant streamwise velocity from reconstruction of the First Eigenfunction. The light surfaces are positive streamwise velocity and the dark surfaces are negative streamwise velocity.

field which is reconstructed from fewer than all modes, small scale detail can be filtered out and the dominant structures identified more clearly. Figure 7 shows the same vorticity field produced from the 100 most energetic modes and suggests that the upper wall is dominated by long streamwise vortices while the shorter, outward tilted vortices play a larger role on the lower wall. These same structures are obviously more difficult to identify from the original flow field which demonstrates one use of partial flow reconstruction using KL modes.

In examining the individual modes, we begin with the most energetic mode, one which contains 13.3% of the flow energy. This mode is characterized by the triplet, $(m,n,q) = (0,1,1)$. It is clear that this mode has no streamwise dependence and its spanwise length-scale is the width of the box. At a specific time, t', we construct the flow $\mathbf{u}^{(0,1,1)}(\mathbf{x},t')$ as described in (17) producing a real valued, incompressible flow field satisfying all boundary conditions. Visualization of this mode is seen in Fig. 8 which shows two surfaces (one
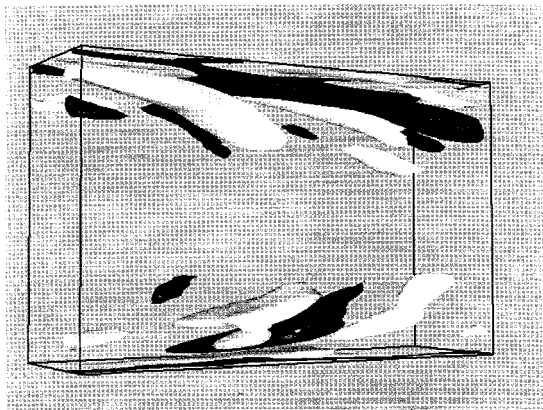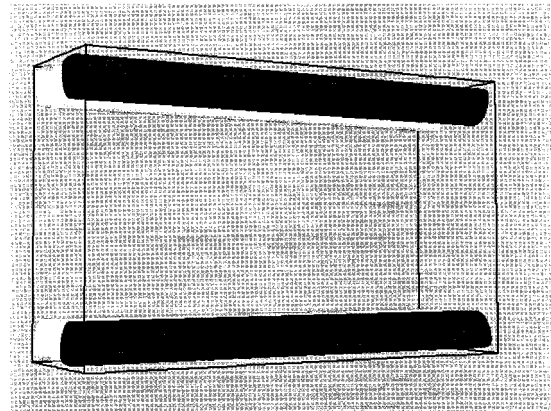

FIG. 7. Surfaces of constant streamwise vorticity from minimal channel reconstructed from the 100 most energetic modes. The light surfaces are positive streamwise vorticity and dark surfaces are negative streamwise vorticity.

positive and one negative) of constant streamwise velocity. From further examinations, the flow field clearly consists of two counter rotating vortices (we use the term vortex in a loose way to imply rolls) which span the length and width of the channel producing a streak spacing of $\lambda^+ = 128$ which is in reasonable agreement with the streak spacing found experimentally.[6] Negative streamwise velocity is found in the regions where the two vortices act to pump fluid away from the wall while positive streamwise velocity is found where the vortices are bringing fluid from the outer flow toward the wall as suggested by Bakewell and Lumley.[36] The magnitude of the streamwise velocity from this mode is largest at $x_2^+ = 15$. It is interesting to observe that in experimental and numerical studies, the peak value of the root mean squared streamwise velocity fluctuation, u_1', is also found at $x_2^+ = 15$.[9,10]

The next most energetic mode is characterized by $(0,1,2)$ and represents 10.5% of the flow energy. It shows a structure similar to the first but with opposite parity, viz. the streamwise velocity of this mode is odd in the wall normal direction. Because all modes with spanwise but no streamwise dependence appear as a collection of long rolls, we will hereafter refer to them as *roll modes*. The analysis of full channel flow[25] also shows the roll modes to be the most energetic ones. The first and second modes in this study have the same size and structure as the $(0,5,1)$ and $(0,5,2)$ modes from the full channel study as explained earlier. Along with roll modes, the only other modes without streamwise dependence are *net flux modes* for which $(m,n) = (0,0)$. These modes vary only in the wall normal direction which vary only in the wall normal direction and are the only modes, along with the mean, which enter into the calculation of the bulk velocity. The net flux modes along with the roll modes together form the entire group of modes without streamwise dependence and are referred to as *kinematically degenerate* modes.[24]

The third most energetic eigenfunction for which $(m,n,q) = (1,1,1)$ does show streamwise dependence. Such streamwise dependent modes have been shown to move at a predictable speed[24] and have been termed *propagating*
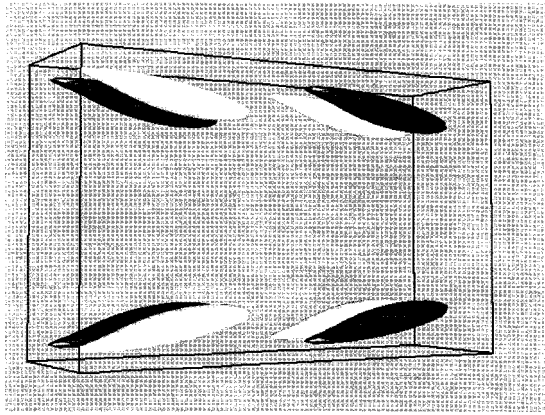
FIG. 9. Surface of constant streamwise velocity from reconstruction of the third eigenfunction. The light surfaces are positive streamwise velocity and the dark surfaces are negative streamwise velocity.
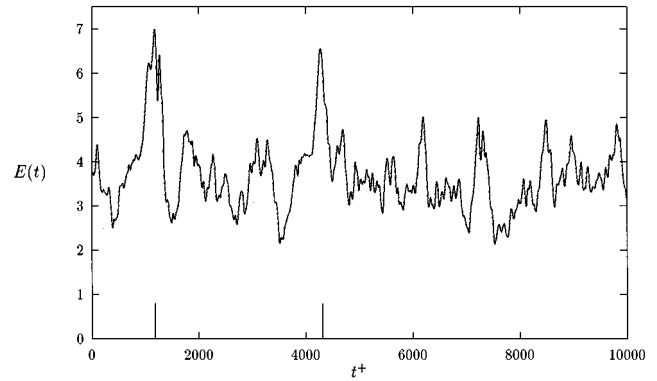

FIG. 10. Energy in the fluctuating portion of the minimal channel flow. The vertical lines denote representative times of event 1 and event 2.

scale structures, leading to the identification of the dominant wall vortices.

C. Flow dynamics and entropy events

Having obtained the dominant KL modes, we now examine how the structures interact over time and what they can reveal about the detailed dynamics of the flow. Using the empirical eigenfunctions from the initial simulation, the flow data from a second simulation is projected onto these eigenfunctions yielding time dependent coefficients, $a_\mathbf{k}(t)$. These coefficients are employed in the formation of a set of dynamic quantities including energy, entropy, and bulk velocity described in Sec. II which are then used along with a computer animation to examine the flow.

The function $E(t)$ (14), which measures the fluctuating energy of the flow, can be calculated directly from the time dependent coefficients $a_\mathbf{k}(t)$. A plot of $E(t)$ is shown in Fig. 10 based on 3025 modes. Most noticeable are the two sharp peaks near the times $t^+ = 1000$ and $t^+ = 4000$, in addition to a number of smaller spikes. Data are presented in the range $0 \leqslant t^+ \leqslant 10{,}000$ for the purpose of clarity. The second simulation is actually carried out to $t^+ = 40\,000$ and similar spiking activity was found throughout the calculation so that the peaks under discussion are typical. The events occurring at $t^+ = 1000$ and $t^+ = 4000$ indicate, respectively, a sharp rise and fall in turbulent activity which are examined in greater detail below. We will hereafter refer to these events as event 1 and event 2.

We also study the degree to which the fluctuating energy is distributed over the modes by monitoring the representational entropy, $S(t)$, (16). (Entropy can be sensitive to the number of modes included. To ensure the accuracy of the trends indicated in Fig. 11 we studied this sensitivity by determining the entropy based on 96.4% and 90.3% of the fluctuating energy. This provided convincing confirmation of the behavior shown in Fig. 11.) Entropy, shown in Fig. 11, shows two noticeable events near the times also at $t^+ = 1000$ and $t^+ = 4000$, with other minor events at other times. A detailed examination of these events shows that the representational entropy drops to its lowest levels early in the event cycle while the energy is growing rapidly. This indicates that during the energy growth portion of the cycle, the energy is distributed over relatively few modes and the flow
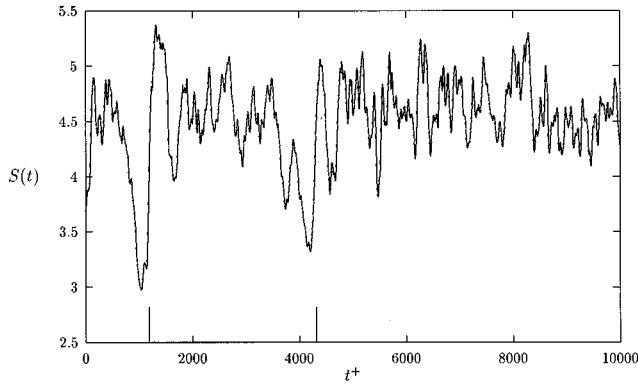
modes. The third mode has a fourfold degeneracy, as shown in (17), which add to form a real valued, incompressible flow field satisfying all boundary conditions. Each such eigenfunction leads to a ''plane wave'' moving at an oblique angle to the constant driving pressure gradient.[23] While an individual eigenfunction moves at an oblique angle, the sum of all four, as shown in (17), produces a structure which moves straight down the channel. Surfaces of constant streamwise velocity for a reconstruction of this mode are shown in Fig. 9. These structures are tilted away from the wall by an angle of 30° (a plot for streamwise vorticity shows an angle of 18°). Similar structures have been noticed in experiment[37] and are defined as quasi-streamwise (outward tilted) vortices.[38] These structures could also be described as an admixture of two types of vortices observed by Bernard, Thomas, and Handler.[8] The first type being the longest vortices whose upstream ends are near the wall and downstream ends are in the outer flow domain and the second being the relatively new vortices which have formed at the wall.

In summary, the minimal channel is a lower dimensional flow than the full channel as expected. More specifically, the KL dimension is directly proportional to computational volume, confirming that dimension is an extensive quantity. Using the KL transform, we are able to directly identify the structures that are thought to be most vital to turbulence self maintenance. This is consistent with the results of Rempfer and Fasel[39] who found the KL procedure to reveal important dynamical structures in the evolving boundary layer. The most energetic mode appears as two counter rotating vortices with a spanwise width on the same order as the streak spacing found in experiment. The largest magnitude of streamwise velocity for this mode occurs at $x_2^+ = 15$, the same position where u_1' is observed to be maximum experimentally. To complement the roll modes, the KL process also identifies a set of propagating modes with a structure similar to the outward tilted or quasi-streamwise structures that move straight down the channel at a steady speed. In addition to examination of the individual modes, the KL reconstruction techniques have proven to be valuable in filtering out small

FIG. 11. Representational entropy of the minimal channel flow, $S(t)$. The vertical lines denote representative times of event 1 and event 2.

FIG. 13. Energy in the roll modes of the minimal channel, $E_r(t)$. The vertical lines denote representative times of event 1 and event 2.

is well organized. A sharp rise in entropy then occurs while energy is still high. This indicates that the energy is redistributed over many modes in a very short time after which the energy decreases. The temporal evolution of the bulk velocity is shown in Fig. 12, and is seen to grow early in the event cycle, reaching its largest values at the times as the entropy is growing rapidly. A suggestion as to how the observed energy redistribution is related to the bulk velocity decrease is presented in Sec. III D.

Because various types of modes (roll and propagating) act in distinctive ways, individual energy contributions for each group are now calculated separately. The roll mode energy represents the contribution to the energy from modes with spanwise but no streamwise dependence and is calculated from the equation

$$E_r(t) = \sum_{\substack{n=-5 \\ n \neq 0}}^{5} \sum_{q=1}^{25} a^{(0,n,q)}(t) \bar{a}^{(0,n,q)}(t), \qquad (19)$$

where $m = 0$ is the streamwise index. A plot of the roll mode energy is seen in Fig. 13 which again shows a spike both at events 1 and 2. A comparison of the roll mode energy and total energy during both events shows that the two quantities rise simultaneously, indicating that the roll modes are the
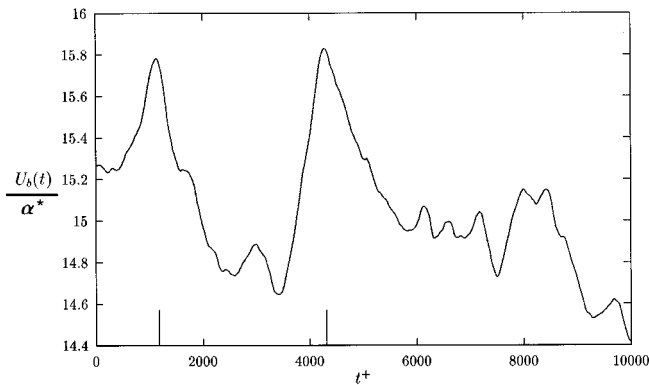
primary contributors to the early growth in the energy. In addition to the roll mode energy, the propagating mode energy, $E_p(t)$, is calculated by

$$E_p(t) = \sum_{\substack{m=-5 \\ m \neq 0}}^{5} \sum_{n=-5}^{5} \sum_{q=1}^{25} a^{(m,n,q)}(t) \bar{a}^{(m,n,q)}(t). \qquad (20)$$

A plot of the propagating mode energy shown in Fig. 14 also shows spikes at the time of the two events. A comparison of the temporal evolution of the roll energy and propagating mode energy shows that the propagating mode energy maximum occurs *after* the the roll mode energy maximum. We also note for the two events, that the roll mode energy rise begins at a time when propagating mode energy is at its minimum. Both of these observations regarding the propagating modes support the findings of Sirovich, Ball, and Handler.[25]

A clearer picture of the first event can be seen in Fig. 15 which shows the temporal behavior of both roll and propa-

FIG. 12. Bulk velocity of the minimal channel flow, $U_b(t)$ scaled with a^*. The vertical lines denote representative times of event 1 and event 2.
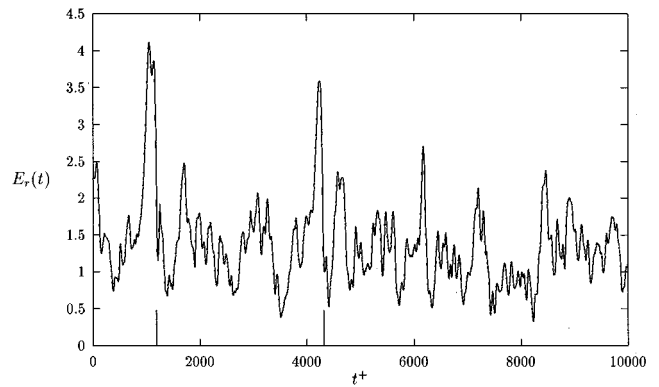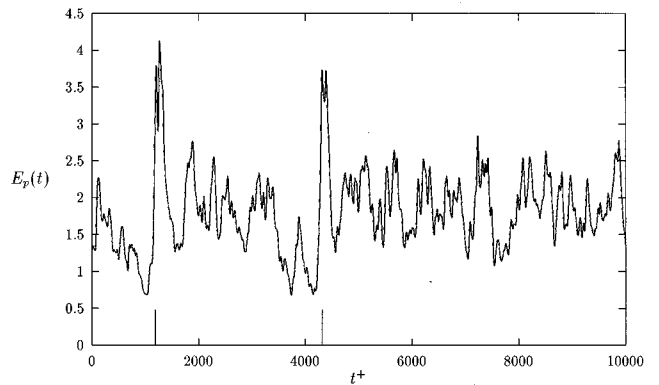

FIG. 14. Energy in the propagating modes of the minimal channel, $E_p(t)$. The vertical lines denote representative times of event 1 and event 2.
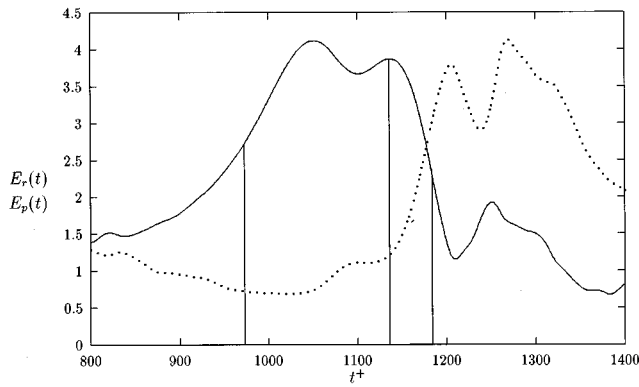
FIG. 15. Energy in roll and propagating modes during the first event, $800 \leqslant t^+ \leqslant 1400$. The solid line represents the roll mode energy and the dots represent the propagating mode energy. The vertical lines represent the times that flow realizations are presented.

FIG. 16. Surfaces of constant streamwise velocity from the fluctuating velocity field at $t^+ = 973$. The light surfaces are positive streamwise velocity and the dark surfaces are negative streamwise velocity.

gating mode energies in the time range $800 \leqslant t^+ \leqslant 1400$. We have also made observations of the bulk velocity and representational entropy through this period. From $t^+ = 800$, when both roll mode and propagating mode energies are small, the roll mode energy rises until $t^+ = 1025$ while the propagating mode energy remains low implying that strong streamwise rolls are formed on the walls. During this same period, entropy steadily decreases reaching its minimum near $t^+ = 1025$ while the bulk velocity rises. The roll mode energy remains large until $t^+ = 1135$ at which time the bulk velocity reaches its peak. Following this time, a number of events occur simultaneously. The roll mode energy energy goes into a sharp decline while the propagating mode energy increases rapidly. (An extensive and detailed energy budget, which is work in progress, confirms that indeed roll energy acts as a source term for the propagating modes.) This indicates that the near wall vortices begin to play a smaller role while the outward tilted, quasi-streamwise modes dominate the activity. In this period, the representational entropy undergoes a sharp increase implying that the energy is redistributed over a large number of modes. The bulk velocity also begins its decrease which suggests that the propagating modes are more effective than the roll modes at transporting momentum to the wall. As time proceeds, the total energy decreases because the smaller scale propagating modes decay at a faster rate than the roll modes. We have examined many periods in which the bulk velocity reaches a maximum and find similar activity in virtually all cases. We now have a description of a cyclical process as seen through roll modes, propagating modes, and representational entropy.

During the time span $800 \leqslant t^+ \leqslant 1400$, a computer animation has been produced which provides a more graphic description of this cyclical process and its related quantities. The animation is generated by viewing surfaces of constant streamwise velocity of the fluctuating flow field $\mathbf{u}(\mathbf{x}, t)$ computed from 3025 modes which account for 96.4% or the total energy. In the time period $800 \leqslant t^+ \leqslant 1025$ two sets of tubes form on the upper and lower wall, as shown in Fig. 16, an

example of the animation taken at $t^+ = 973$. The image shows two tubes on the upper wall with the lower wall structures still in the beginning stages of development. The tubes remain dominant until $t^+ = 1135$ while the propagating mode energy slowly grows. A similar plot of streamwise velocity at this time is seen in Fig. 17 which shows well developed structures on the top and bottom walls. We also see wave-like disturbances which propagate down the channel as shown by animation. At this time the bulk velocity is near its maximum, the entropy is at its minimum, and the roll and propagating modes are on the verge of an energy exchange. As seen in Fig. 15, the propagating mode energy immediately rises increasing the magnitude of these wave-like structures which is a phenomena similar to that reported by Reynolds et al.[5] just before the destruction of the rolls. The final realization is taken at $t^+ = 1184$ and can be seen in Fig. 18. This plot shows a surface extending away from the roll. Evidently we are witnessing the breakup of rolls into smaller scale structures. These small scale structures experience a larger degree of viscous dissipation than the well organized
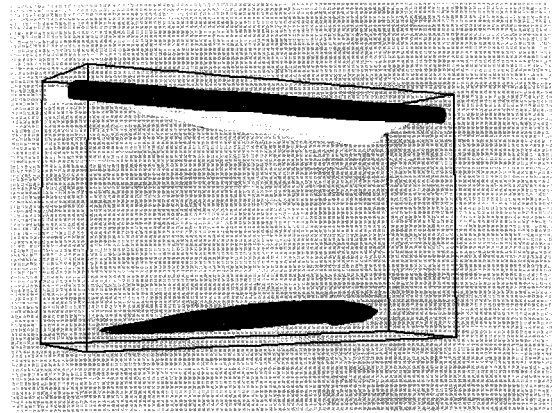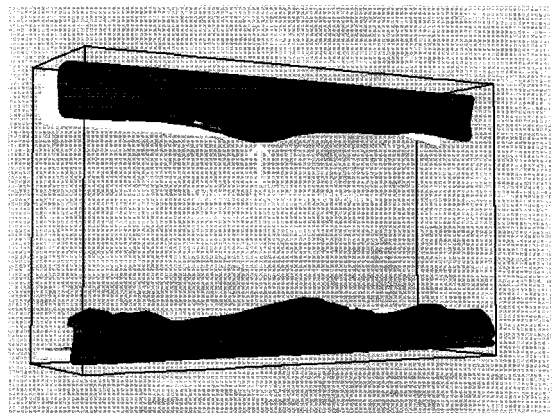

FIG. 17. Surfaces of constant streamwise velocity from the fluctuating velocity field at $t^+ = 1136$. The light surfaces are positive streamwise velocity and the dark surfaces are negative streamwise velocity.
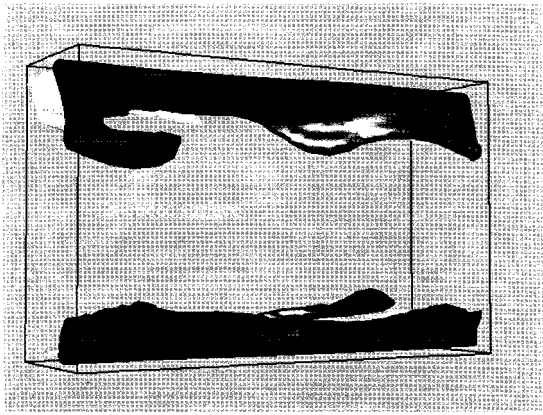
Phys. Fluids, Vol. 9, No. 4, April 1997

Webber, Handler, and Sirovich   1063

FIG. 18. Surfaces of constant streamwise velocity from the fluctuating velocity field at $t^+ = 1184$. The light surfaces are positive streamwise velocity and the dark surfaces are negative streamwise velocity.

FIG. 20. The full Reynolds stress profile scaled by u_τ^2 before and after the energy exchange. The solid line represents the profile at $t^+ = 1125$ and the dots represent the profile at $t^+ = 1210$.

wall structures leading to a decrease in total energy. Our interpretation is that Fig. 17 shows a highly energetic and organized wall-bounded structure shortly before its breakup, and we associate this breakup with what has been termed a burst.

D. Reynolds stress decomposition

In addition to the temporal behavior of the roll modes and propagating modes, we investigate the independent contributions they make to the average Reynolds stress (see the Appendix). By averaging the Navier–Stokes equations over the two homogeneous directions along with time, we see that the pressure gradient is balanced by the viscous shear stress, $(1/R_\tau)(d^2/dx_2^2) U$, and the gradient of Reynolds stress, $(d/dx_2) \overline{u_1 u_2}(x_2)$. Here, we investigate how the various groups of modes contribute to the transport of momentum averaged over time, and what this reveals about momentum transport at various stages of the events.

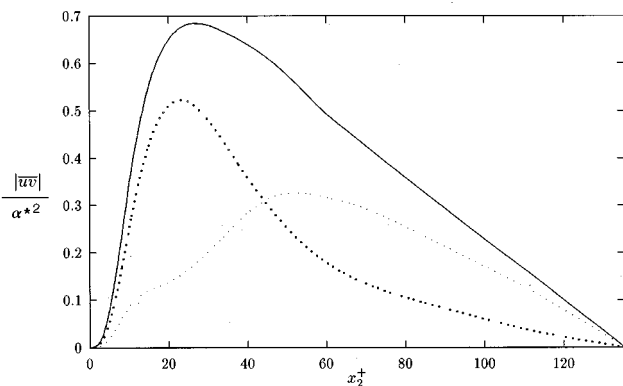A plot of the roll mode contribution to the Reynolds stress (A5), the propagating mode contribution to the Reynolds stress (A6), and their sum is shown in Fig. 19. From this result, we see that the roll modes dominate the Reynolds stress in the buffer layer reaching their peak at $x_2^+ = 23$. On the other hand, the propagating modes show a greater presence in the region further from the wall reaching a peak at $x_2^+ = 52$, well into what would in a normal channel be the log layer.

We now will examine the total Reynolds stress profiles which are calculated at specific times with averaging done in the streamwise and spanwise directions. Figure 20 shows two profiles, the first at $t^+ = 1125$, just before the energy transfer from roll to propagating modes of event 1, and the second at $t^+ = 1210$, immediately after the transfer. We note that these profiles represent the entire Reynolds stress, and no separation into various groups of modes has occurred. At $t^+ = 1125$, the bulk velocity is rising and the majority of energy is in the roll modes. At this time the Reynolds stress near the wall is greater than the time averaged values, and the magnitudes in the channel center are less than the time averaged values. The profile calculated at $t^+ = 1210$, when the propagating mode energy has reached its first peak, shows that the Reynolds stress is more active in the center of the channel which results in a decline in bulk velocity. This result shows that the propagating modes are more effective at transporting momentum to the channel walls thereby reducing the bulk velocity. Similar profiles are found at event 2, $4000 \leqslant t^+ \leqslant 4600$.

IV. CONCLUSIONS

We have simulated a minimal channel flow using a constant driving pressure gradient which has yielded flow statistics which are similar to empirical results. The computed KL dimension ($D_{KL} = 658$) for the minimal channel was smaller than the KL dimension of the full channel ($D_{KL} = 4186$) by about the same factor as the ratio of the two channel volumes, confirming that dimension is an extensive variable.

The most energetic flow modes identified by the KL process have a strong similarity to structures seen in the experiment. A reconstruction of the most energetic mode showed two counter rotating vortices with a streak spacing of $\lambda^+ = 128$, one box width of the channel, which is close to the standard streak spacing of $\lambda^+ = 100$. The largest magnitude

FIG. 19. The average Reynolds stress in the minimal channel scaled by u_τ^2. The solid line represents the entire Reynolds stress, the large dots represent the Reynolds stress from the roll modes, and the smaller dots represent the Reynolds stress from the propagating modes.
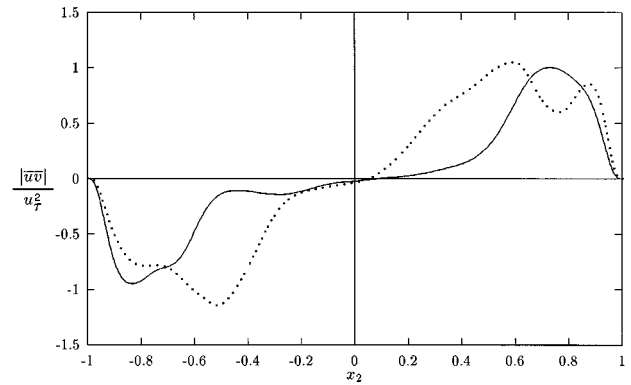
of streamwise velocity for this mode is at $x_2^+ = 15$, which agrees with experimental and other numerical simulations. The propagating modes are tilted away from the wall at an angle, in a manner similar to quasi-streamwise vortices seen in both experiment and numerical simulation, and travel straight down the channel.

The minimal channel flow in combination with the KL procedure is extremely effective for revealing flow activity through the examination of the dynamic quantities. The minimal channel will have at most one pair of counter rotating vortices on each wall going through the process of formation, growth, or destruction. A larger channel, on the other hand, will have multiple vortices at various stages of the process. The dynamic quantities calculated from the minimal channel will therefore present a clearer picture of the life of these vortices. The temporal evolution of roll mode energy, propagating mode energy, representational entropy, and bulk velocity show interesting and consistent patterns during periods of turbulent bursts. We observed that representational entropy growth occurs simultaneously with the transfer of energy from the roll to the propagating modes all at a time of peak bulk velocity. The bulk velocity rises at times of low propagating mode energy and begins to decrease after the energy has been transferred from the roll modes to the propagating modes. An animation performed at this same time shows the formation and destruction of strong wall-bounded rolls.

Finally, this work has demonstrated how roll and propagating modes make independent contributions to the Reynolds stress with the roll modes dominating the profile near the walls and the propagating modes generating larger values towards the channel center. Reynolds stress profiles calculated at specific times before and after the exchange of energy from roll to propagating modes of the events show that the Reynolds stress goes from a wall dominated quantity to a center quantity during the exchange causing the bulk velocity to begin its decrease.

ACKNOWLEDGMENTS

APPENDIX: STRESS ANALYSIS

By averaging the Navier–Stokes equations over the two homogeneous directions as well as time, we are left with the relationship

$$0 = 1 - \frac{d}{dx_2}\overline{u_1 u_2}(x_2) + \frac{1}{R_\tau}\frac{d^2}{dx_2^2}U(x_2). \tag{A1}$$

The first term, 1, is a product of the driving pressure gradient and is counteracted by the viscous shear stress, $(1/R_\tau) \times (d^2/dx_2^2)U(x_2)$, and the gradient of the Reynolds stress, $(d/dx_2)\overline{u_1 u_2}(x_2)$. We note that the viscous shear stress is a product of the mean flow and the Reynolds stress is a product of the fluctuating portion of the flow.

To analyze the Reynolds stress by Fourier wave pair (m,n) we first decompose the fluctuating flow field into such pairs,

$$\mathbf{u}(x_1,x_2,x_3,t) = \sum_{m=-M/2}^{M/2-1}\sum_{n=-N/2}^{N/2-1}\hat{\mathbf{u}}(x_2,m,n,t)$$
$$\times e^{2\pi i m x_1/L_1}e^{2\pi i n x_3/L_3}. \tag{A2}$$

Next, we recognize that the flow field is real allowing u_2 to be written as

$$u_2 = \sum_{m'=-M/2}^{M/2-1}\sum_{n'=-N/2}^{N/2-1}\hat{u}_2 e^{2\pi i m' x_1/L_1}e^{2\pi i n' x_3/L_3} = \overline{u_2}$$
$$= \sum_{m'=-M/2}^{M/2-1}\sum_{n'=-N/2}^{N/2-1}\overline{\hat{u}_2}e^{-2\pi i m' x_1/L_1}e^{-2\pi i n' x_3/L_3}. \tag{A3}$$

Using these expansions, the Reynolds stress is calculated by the equation

$$\overline{u_1 u_2} = \frac{1}{TL_1L_3}\int_0^T\int_0^{L_1}\int_0^{L_3}u_1(x_1,x_2,x_3,t)u_2(x_1,x_2,x_3,t)dx_3dx_1dt$$

$$= \frac{1}{TL_1L_3}\int_0^T\sum_{m=-M/2}^{M/2-1}\sum_{n=-N/2}^{N/2-1}\sum_{m'=-M/2}^{M/2-1}\sum_{n'=-N/2}^{N/2-1}\hat{u}_1\overline{\hat{u}_2}\int_0^{L_1}\int_0^{L_3}e^{-2\pi i x_1(m-m')/L_1}e^{-2\pi i x_3(n-n')/L_3}dx_3dx_1dt$$

$$= \frac{1}{T}\int_0^T\sum_{m=-M/2}^{M/2-1}\sum_{n=-N/2}^{N/2-1}\sum_{m'=-M/2}^{M/2-1}\sum_{n'=-N/2}^{N/2-1}\hat{u}_1(x_2,m,n,t)\overline{\hat{u}_2}(x_2,m',n',t)\delta_{mm'}\delta_{nn'}dt$$

$$= \sum_{m=-M/2}^{M/2-1}\sum_{n=-N/2}^{N/2-1}\frac{1}{T}\int_0^T\hat{u}_1(x_2,m,n,t)\overline{\hat{u}_2}(x_2,m,n,t)dt. \tag{A4}$$

Phys. Fluids, Vol. 9, No. 4, April 1997

Webber, Handler, and Sirovich   1065

Although Reynolds stress is computed from a nonlinear product, each wave pair (m,n) makes an independent contribution to it. In addition, the groups of wave pairs, roll modes and propagating modes, will each make independent contributions which collectively account for the entire Reynolds stress. The roll mode contribution to the Reynolds stress is calculated by the equation

$$\overline{u_1 u_{2r}} = \sum_{\substack{n=-N/2 \\ n \neq 0}}^{N/2-1} \frac{1}{T} \int_0^T \hat{u}_1(x_2,0,n,t)\overline{\hat{u}_2}(x_2,0,n,t)dt, \quad (A5)$$

and the propagating mode contribution is calculated by

$$\overline{u_1 u_{2p}} = \sum_{\substack{m=-M/2 \\ m \neq 0}}^{M/2-1} \sum_{n=-N/2}^{N/2-1} \frac{1}{T} \int_0^T \hat{u}_1(x_2,m,n,t)$$
$$\times \overline{\hat{u}_2}(x_2,m,n,t)dt. \quad (A6)$$

Using the continuity equation and boundary conditions, we can show that $\hat{u}_2(x_2,0,0,t)=0$, therefore the net flux modes make no contribution to the Reynolds stress.

[1] J. Jiménez and P. Moin, ''The minimal flow unit in near-wall turbulence,'' J. Fluid Mech. **225**, 213 (1991).

[2] C. R. Smith, J. D. A. Walker, A. H. Haidari, and U. Sobrun, ''On the dynamics of near-wall turbulence,'' Philos. Trans. R. Soc. London Ser. A, **336**, 134 (1991).

[3] R. F. Blackwelder and R. E. Kapan, ''On the wall structure of the turbulent boundary layer,'' J. Fluid Mech. **76**, 89 (1976).

[4] J. O. Hinze, *Turbulence* (McGraw-Hill, New York, 1975).

[5] S. J. Kline, W. C. Reynolds, F. A. Schraub, and P. W. Runstadler, ''The structure of turbulent boundary layers,'' J. Fluid Mech. **30**, 741 (1967).

[6] C. R. Smith and S. P. Metzler, ''The characteristics of low-speed streaks in the near-wall region of a turbulent boundary layer,'' J. Fluid Mech. **129**, 27 (1983).

[7] D. G. Bogard and W. G. Tiederman, ''Burst detection with single-point velocity measurements,'' J. Fluid Mech. **162**, 389 (1986).

[8] P. S. Bernard, J. M. Thomas, and R. A. Handler, ''Vortex dynamics and the production of Reynolds stress,'' J. Fluid Mech. **253**, 385 (1993).

[9] T. Wei and W. W. Willmarth, ''Reynolds-number effects on the structure of turbulent channel flow,'' J. Fluid Mech. **204**, 57 (1989).

[10] J. Kim, P. Moin, and R. Moser, ''Turbulence statistics in fully developed channel flow at low Reynolds number,'' J. Fluid Mech. **177**, 133 (1987).

[11] H. Tennekes and J. L. Lumley, *A First Course in Turbulence* (MIT Press, Cambridge, 1972).

[12] J. Lumley, *Stochastic Tools in Turbulence* (Academic Press, New York, 1970).

[13] K. Karhunen, ''Zur Spektraltheorie stochastischer Prozesse,'' Ann. Acad. Sci. Fennicae, Ser. A **1**, 34 (1946).

[14] M. Loéve, *Probability Theory* (Van Nostrand, Princeton, NJ, 1955).

[15] E. Schmidt, ''Zur Theorie der linearen und nichtlinearen Integralgleichungen. I Teil: Entwicklung willkulicher Funktion nach Systemen vorgeschriebener,'' Mathematische Annalen, 1907.

[16] L. Sirovich and R. Everson, ''Management and analysis of large scientific datasets,'' The Int. J. Supercomput. Appl. **6**, 50 (1992).

[17] K. Fukanaga, *Introduction to Statistical Pattern Recognition* (Academic, New York, 1972).

[18] R. W. Preisendorfer, *Principal Component Analysis in Meteorology and Oceanography* (Elsevier, New York,1988).

[19] E. N. Lorenz, ''Empirical orthogonal functions and statistical weather prediction,'' Department of Metrology, MIT, 1, Statistical Forecasting Project, Cambridge, MD, 1956.

[20] L. Sirovich, ''Turbulence and the dynamics of coherent structures, Part I: Coherent structures,'' Q Appl. Math. **XLV**, 561 (1987).

[21] L. Sirovich, ''Turbulence and the dynamics of coherent structures, Part II: Symmetries and transformations,'' Q. Appl. Math. **XLV**, 573 (1987).

[22] P. Moin and R. Moser, ''Characteristic-eddy decomposition of turbulence in a channel,'' J. Fluid Mech. **200**, 471 (1989).

[23] L. Sirovich, K. S. Ball, and L. R. Keefe, ''Plane waves and structures in turbulent channel flow,'' Phys. Fluids A **2**, 2217 (1990).

[24] K. S. Ball, L. Sirovich, and L. R. Keefe, ''Dynamical eigenfunction decomposition of turbulent channel flow,'' Int. J. Numer. Meth. Fluids **12**, 585 (1991).

[25] L. Sirovich, K. S. Ball, and R. A. Handler, ''Propagating structures in wall-bounded turbulent flows,'' Theor. Comput. Fluid Dyn. **2**, 307, (1991).

[26] L. Sirovich and J. D. Rodriguez, ''Coherent structures and chaos: A model problem,'' Phys. Lett. A **120**, 5 (1987).

[27] L. Keefe, P. Moin, and J. Kim, ''The dimension of attractors underlying periodic turbulent Poiseuille flow,'' J. Fluid Mech. **242**, 1 (1992).

[28] G. Berkooz, P. Holmes, and J. L. Lumley, ''On the relation between low-dimensional models and the dynamics of coherent structures in the turbulent wall layer,'' Theor. Comput Fluid Dyn. **4**, 255 (1993).

[29] L. Sirovich and X. Zhou, ''Dynamical model of wall-bounded turbulence,'' Phys. Rev. Lett. **72**, 340 (1994).

[30] M. J. Walsh, ''Riblets,''*Progress in Astronautics and Aerodynamics*, edited by D. Bushnell and J. Narasimha (AIAA, New York, 1990), Vol. 123.

[31] J. L. Lumley, ''Drag reduction by additives,'' Ann. Rev. Fluid Mech. **1**, 367 (1969).

[32] R. A. Handler, E. Levich, and L. Sirovich, ''Drag reduction in turbulent channel flow by phase randomization,'' Phys. Fluids A **5**, 686 (1993).

[33] R. A. Handler, E. W. Hendricks, and R. I. Leighton, ''Low Reynolds number calculation of turbulent channel flow: A general discussion,'' NRL Memorandum Report 6410, 1989.

[34] R. D. Dean, ''Reynolds number dependence of skin friction and other bulk flow variables in two-dimensional rectangular duct flow,'' J. Fluids Eng. **100**, 215 (1978).

[35] L. Sirovich, ''Empirical eigenfunctions and low dimensional systems,'' *New Perspectives in Turbulence* (Springer-Verlag, 1991), pp. 139–163.

[36] H. P. Bakewell and J. L. Lumley, ''Viscous sublayer and adjacent wall region in turbulent pipe flow,'' Phys. Fluids **10**, 1880 (1967).

[37] C. R. Smith and S. P. Schwartz, ''Observation of streamwise rotation in the near-wall region of a turbulent boundary layer,'' Phys. Fluids **26**, 641 (1983).

[38] S. K. Robinson, ''Coherent motions in the turbulent boundary layer,'' Annu. Rev. Fluid Mech. **23**, 601 (1991).

[39] D. Rempfer and H. Fasel, ''Evolution of three-dimensional coherent structures in a flat-plate boundary layer,'' J. Fluid Mech. **260**, 351 (1994).